EUROPEAN FUSION DEVELOPMENT AGREEMENT

EFDA–JET–PR(03)44

J.-S. Lönnroth, V.V. Parail, G.T.A. Huysmans, G. Saibene, H.R. Wilson,
S.Sharapov, G. Corrigan, D. Heading, R.Sartori, M. Bécoulet
and JET EFDA contributors

Predictive Transport Modelling of H-mode Plasmas with Type II ELMs

Predictive Transport Modelling of H-mode Plasmas with Type II ELMs

J.-S. Lönnroth[1], V.V. Parail[2], G.T.A. Huysmans[3], G. Saibene[4], H.R. Wilson[2], S. Sharapov[2], G. Corrigan[2], D. Heading[2], R.Sartori[4], M. Bécoulet[3] and JET EFDA contributors*

[1]Association EURATOM-Tekes, Helsinki University of Technology, P.O. Box 2200, 02015 HUT, Finland
[2]EURATOM/UKAEA Fusion Association, Culham Science Centre, Abingdon, Oxon, OX14 3DB, UK
[3]Association EURATOM-CEA, CEA Cadarache, DRFC, 13108 Saint-Paul-Lez-Durance, France
[4]EFDA Close Support Unit, c/o Max Planck Institut für Plasmaphysik, Boltzmannstrasse2, 85748 Garching, Germany
** See annex of J. Pamela et al, "Overview of Recent JET Results and Future Perspectives", Fusion Energy 2000 (Proc. 18th Int. Conf. Sorrento, 2000), IAEA, Vienna (2001).*

Preprint of Paper to be submitted for publication in
Plasma Physics and Controlled Fusion

ABSTRACT.
Mixed type I-II ELMy H-mode, a mode operation with small frequent type II ELMs interrupted by occasional large type I ELMs, has been observed in various experimental situations. Starting from MHD stability analysis of predictive transport simulations constituting a scan in the level of external neutral gas puffing, this paper presents a model for mixed type I-II ELMy H-mode as well as for pure type I, type II and type III ELMy H-mode. The 1.5 D core transport code JETTO has been equipped with an implementation of the model. Some justification from theory and numerical analysis is given for the best representation of type II ELMs. It is demonstrated through predictive transport simulations with JETTO that the model can reproduce the experimental dynamics of mixed type I-II ELMy H-mode. A simulation of mixed type I-II ELMy H-mode is compared with reference simulations of pure type I, type II and type III ELMy H-mode in terms of ELM characteristics and confinement and the differences are explained. Apart from in discharges with strong gas puffing, a topic discussed at the beginning of the paper, type II ELMs have also been experimentally observed mainly in discharges with a quasi double null magnetic configuration, in discharges with high poloidal β_p (ratio of the total pressure to the kinetic pressure) and in discharges with a combination of high edge safety factor q_{95} and high triangularity δ. By means of MHD stability analysis performed on interpretative or predictive JETTO simulations, each of these situations is shown to be favourable for type II ELMs according to the ELM model used in the paper.

1. INTRODUCTION

The high confinement mode (H-mode) offers a promising operational regime for tokamak fusion devices. A characteristic feature of the H-mode is the formation of an Edge Transport Barrier (ETB) in the outer region of the plasma, just inside the magnetic separatrix. The reduction of transport within the ETB leads to large density and temperature gradients in this region, causing it to stand out as a "pedestal" in the density and temperature profiles. The H-mode is generally accompanied by short periodic bursts of particles and energy at the plasma edge triggered by MagnetoHydroDynamic (MHD) instabilities and known as Edge Localized Modes (ELMs). There are several effects of ELMs on plasma performance. ELMs have the beneficial effect of transporting density and impurities over the pedestal region. ELM-free plasmas usually terminate due to the accumulation of im-purities, because particles and especially impurities are extremely well confined in them. However, the ELM-related energy loss, although only a small fraction of the total plasma energy, can produce high peak heat loads on the divertor plates, which can become a serious problem in large tokamaks. Another effect of ELMs is to limit the pressure gradient within the pedestal and at the top of it, thereby affecting confinement. The ELMy H-mode is envisaged as a reference operational scenario for the International Thermonuclear Experimental Reactor (ITER) and other future burning plasma devices.

Different ELM types have been identified or defined. Type I or "giant" ELMs are the most commonly observed type of ELMs in plasmas with large enough heating power. They are large events capable of removing up to 10% of the plasma energy with a repetition frequency that increases

with increased radial power flux across the last closed flux surface. Type III ELMs, which are small and frequent, are often seen slightly above the H-mode threshold power. Type III ELMs are generally characterized by an ELM frequency that decreases with power [1]. Type II ELMs resemble type III ELMs, but are generally even tinier and more frequent. Sometimes MHD activity in type II ELMy H-mode has a continuous rather than an intermittent character. The distinction between ELM types II and III, both of which are commonly referred to as "grassy ELMs", is based on their different effects on plasma performance. The definitions used in this paper will be explained further on. Type II ELMs often occur in a mixed type I-II ELMy H-mode, i.e. a mode of operation with tiny, frequent type II ELMs interrupted by occasional large type I ELMs. [2, 3]

Frames (a), (b) and (c) in Fig. 1 illustrate the characteristic Dα emission signal as a function of time of three different ELMy H-mode discharges: 53298, which is a pure type I ELMy H-mode discharge, 53299, which is a mixed type I-II ELMy H-mode discharge and 52739, which is a pure type III ELMy H-mode discharge. Pure type II ELMy H-mode has never been observed at JET. In general, pure type I ELMy H-mode is characterized by slightly better confinement than mixed type I-II ELMy H-mode and much better confinement than pure type III ELMy H-mode. This is illustrated in frame (d) in Fig.1, which shows the confinement factor H98Y [4] as a function of time for the three aforementioned discharges.

This paper focuses on plasmas with type II ELMs. Type II ELMs have the advantage of producing much smaller heat and particle loads on the divertor plates than type I ELMs, while still offering good confinement properties. The energy lost in a single type II ELM is significantly smaller than in a single type I ELM, which means that the pulsed power exhaust due to type I ELMs can be completely avoided in operation with pure type II ELMs. Type II ELMy H-mode operation can thus potentially help to solve the problem of too strong erosion of the divertor and strike point regions, one of the remaining concerns about H-mode operation in future devices.

The paper is structured as follows. In Sec. 2, the occurrence of ELMy H-modes with type II ELMs is discussed. Section 3 contains a brief overview of the simulation codes used in this work. Then, in Sec.4, a model for type I, type II and type III ELMs is presented using a scan in external neutral gas puffing as an example illustrating qualitatively different situations corresponding to different types of ELMy H-mode. The implementation of the model is discussed in Sec.5. Section 6 elaborates on the width of type II ELMs and the ballooning modes supposed to drive them. The main results of predictive transport mod-elling with the ELM model are presented in Sec.7. In Sec8., the effect of the magnetic configuration on the occurrence of type II ELMs is investigated, in Sec. 9 the effect of the poloidal (ratio of the total pressure to the magnetic pressure), in Sec. 10 the effect of the edge safety factor and in Sec.11 the effect of triangularity. The paper is concluded with a summary and discussion in Sec.12.

2. OCCURRENCE OF TYPE II ELMS

Pure type II ELMy H-modes and / or mixed type I-II ELMy H-modes have been observed in

several different situations. The perhaps best example in JET is the occurrence of type II ELMs in discharges with moderately strong gas puffing. From experiments, it is known that plasma easily accommodates modest gas puffing, e.g. a neutral influx of $\Gamma = 3\times10^{22}$ s^{-1} in the case of JET. Higher levels of gas puffing can trigger a transition from pure type I ELMy H-mode to mixed type I-II ELMy H-mode and eventually a transition to pure type III ELMy H-mode [5]. The transition from the type I ELM regime is accompanied by a dramatic increase in the ELM frequency and a deterioration of plasma confinement. The deterioration of confinement is usually modest for a transition to type II ELMy H-modes and more significant for a transition to type III ELMy H-mode. Strong gas puffing is associated with high edge density, which seems to be a common feature also in other scenarios with type II ELMs. Pure type II ELMy H-modes as well as mixed type I-II ELMy H-modes have been observed in plasmas with high poloidal beta β_p in JT-60U [6]. Here, β is the ratio of the total pressure to the magnetic pressure. Like high edge density, high β_p seems to be a common feature of discharges with type II ELMs. At JT-60U, high β_p is a necessary condition for access to type II ELM regimes, so that if $\beta_p < 1.7$ there is no access to type II ELMs. Pure type II and mixed type I-II ELMy H-modes have also been observed in JT-60U discharges with high safety factor q at the edge and high triangularity δ [7, 8]. Mixed type I-II ELMy H-modes typically occur for $q_{95} \gtrsim 4$ and $\delta \gtrsim 0.3$ and pure type II ELMy H-modes for $q_{95} \gtrsim 5$ and $\delta \gtrsim 0.45$ in JT-60U. Here, q_{95} is the safety factor at the magnetic surface $\psi = 0.95$,where is the poloidal flux co-ordinate. Pure type II ELMy H-modes as well as mixed type I-II ELMy H-modes have been observed in ASDEX Upgrade in quasi double null discharges [9, 10], i.e. in discharges with a magnetic configuration having a second X-point in the proximity of the plasma. Type II ELMs in quasi double null configurations have been reported for a rather broad range of triangularities and edge safety factors, especially at high densities.

3. SIMULATION CODES

In this paper, transport simulations of the time evolution of the plasma parameters have been carried out using the 1.5D JETTO transport code [11] equipped with a new ELM model. The codes HELENA and MISHKA [12] have been used for MHD stability analysis.

3.1 JETTO

In simulations with JETTO, the empirical JET transport model, a mixed Bohm / gyro-Bohm model [14], has been used. The Bohm and the gyro-Bohm terms in the JET model are given by relevant contributions to the diffusivity [15]. The Bohm term in the model includes both electron and ion transport as well as a non-local factor accounting for the instantaneous effect of perturbations starting at the plasma edge, such as ELMs. The gyro-Bohm term makes its largest contribution in the deep core. The model also includes neo-classical transport from NCLASS [15].

JETTO has a fixed boundary solver of the Grad-Shafranov equation called ESCO, which generates equilibria consistent with the predicted temperature and pressure profiles in the core. JETTO explicitly takes the region with the ETB into account. It is assumed that anomalous transport is completely

suppressed within the ETB, so that the only remaining transport is neo-classical. The transport coefficients are thus suddenly reduced to a constant neo-classical level from the top of the ETB to the plasma edge. The assumption of uniformity of neo-classical transport within the ETB is a reflection of the fact that the pedestal width is usually of the order of the ion orbit width, implying limited variation of neo-classical transport across the barrier. The width of the ETB can be considered either a fixed parameter or be calculated using recently developed theory-based models [16]. In this work, a fixed ETB width of 3 cm is used. The effect of letting the pedestal width vary is studied in Ref. [17].

3.2 MHD STABILITY CODES

In the work presented in this paper, MHD stability analysis has been carried out using the codes HELENA and MISHKA. HELENA takes plasma profiles and equilibrium in-formation generated by JETTO and evaluates stability against ideal n = 1 ballooning modes. HELENA also produces an equilibrium with better resolution, which can then be used by MISHKA as input. MISHKA evaluates stability against finite n kink, peeling and ballooning modes. For efficiency, a version of the MISHKA code called MISHKA-1 has been used in this paper. This is an ideal MHD version of MISHKA not taking into account drift effects.

4. DEFINITION OF ELM TYPES EXEMPLIFIED BY A SCAN IN THE LEVEL OF EXTERNAL NEUTRAL GAS PUFFING

It is broadly believed that ELMs are controlled by a combination of ballooning and peeling modes [18, 19, 20, 21, 22]. The definitions of different ELM types used in this paper are related to the different ballooning stability limits associated with $n = \infty$ and finite n ballooning modes in different regions of parameter space. These definitions will be explained by considering three predictive transport simulations with different levels of external neutral gas puffing, which represent three qualitatively different situations with respect to MHD stability. Transitions between these situations are believed to correspond to transitions between different types of ELMs. This subject has already been extensively discussed in Ref. [13], but the results will be reviewed here, because in addition to illustrating how different ELM types are defined in the present model they include a situation with type II ELMs.

External neutral gas puffing affects MHD stability through a sequence of causalities: Due to poor penetration of neutrals through the Scrape-Off Layer (SOL), increasing gas puffing leads to increasing edge density, which in turn results in increasing collisionality at the edge. As a consequence of increasing collisionality at the edge, the bootstrap current decreases. A decrease in the bootstrap current causes an in increase in magnetic shear at the edge, which directly influences MHD stability sensitively.

Figure 2 shows MHD stability diagrams with the normalized pressure gradient on the horizontal axis and magnetic shear s on the vertical axis for three predictive JETTO simulations with different levels of gas puffing: $\Gamma = 0$, $\Gamma = 4\times10^{22}\ s^{-1}$ and $\Gamma = 1\times10^{23}\ s^{-1}$. In this paper, the following normalization is used for α:

$$\alpha = - \frac{2\mu_0 = q^2}{B_0^2 \in} \frac{dp}{d\rho}. \quad (1)$$

Here, μ_0 is permeability of vacuum, q is the safety factor, B_0 is the magnetic field on the magnetic axis, $\in$ is the inverse aspect ratio, p is the pressure and ρ is the toroidal flux co-ordinate. In predictive simulations, the plasma profiles, e.g. density, temperature and current, are calculated subject to boundary conditions using the given transport model. Here, the JETTO runs have been performed using the geometry of the high triangularity ($\delta = 0.5$) JET Pulse No: 53298. For the MHD stability analysis, a suite consisting of the HELENA and MISHKA codes has been used. The codes have been run on a series of equilibria obtained by repeatedly changing the edge pressure gradient and edge current within the ETB. Each combination of edge pressure gradient and edge current translates into a given combination of α and s as a function of the flux surface. For each combination, the mode number of the most unstable kink, peeling or finite n ballooning mode ($n \leq 14$) as calculated by MISHKA has been printed onto the plots, which correspond to the magnetic surface $\rho = 0.95$. Whenever no instabilities have been found, the relevant location on the plot has been left blank. In addition, the $n = \infty$ ballooning instabilities as calculated by HELENA have been marked with crosses on the plots. One can easily make out four distinct regions on the plots, each of which has been marked with a different shade of grey: a region with no instabilities, a region in which the low n (n . 8) kink instability is dominant, a region in which the medium n ($8 \lesssim n \lesssim 14$) ballooning / peeling instability dominates and the $n = \infty$ ballooning unstable region. In most cases, the latter two regions partially overlap each other. Finally, the plots show the location of the operational point, i.e. the point with unperturbed edge current and edge density, for a few different magnetic surfaces. Strictly speaking, separate plots should be presented for different flux surfaces in order to show how the stability of the operational point evolves. However, because the unstable region evolves relatively little with the magnetic surface in these cases, the operational point can be plotted as a function of the magnetic surface onto a single plot without qualitative error, as has been done here.

In frame (a) in Fig. 2 corresponding to the lowest level of gas puffing in the scan ($\Gamma = 0$), the operational point is located in the second $n = \infty$ ballooning stability region for all magnetic surfaces within the ETB. Even though magnetic shear increases close to the edge, the operational point stays in the second ballooning stability region. The maximum operational α is defined by the finite n ballooning stability limit at $\alpha \approx 6$. An ELM is triggered when the pressure gradient exceeds this limit. To be specific, an ELM resulting from a violation of the finite n ballooning stability limit is defined as a type I ELM in the model used in this paper. Consequently, the situation shown in frame (a) in Fig.2 corresponds to a pure type I ELMy H-mode.

In frame (b) in Fig.2 corresponding to the intermediate level of gas puffing in the scan ($\Gamma = 4 \times 10^{22}$ s^{-1}), the operational point is located in the second ballooning stability region for magnetic surfaces close to the top of the ETB, but it becomes $n = \infty$ ballooning unstable for magnetic surfaces just inside the separatrix. This means that stability at the very edge is limited by the first $n = \infty$ ideal

ballooning stability limit, whereas stability deeper inside the ETB is still determined by the finite *n* ballooning instabilities. The relevant stability limits are the first ballooning stability limit at $\alpha \approx 3.5$ for the very edge and the finite *n* ballooning stability limit $\alpha \approx 6$ for the rest of the ETB. According to the present model, type I ELMs again result from violations of the finite *n* ballooning stability limit in the inner part of the ETB. However, violations of the first ballooning stability limit at the outermost flux surfaces are interpreted to result in type II ELMs at the edge. Therefore, the situation shown in frame (b) in Fig.2 corresponds to a mixed type I-II ELMy H-mode. Analogously, a pure type II ELMy H-mode occurs when the pressure gradient in the inner part of the ETB never builds up to the critical level defined by the finite n ballooning stability limit, but the outermost edge is still unstable against $n = \infty$ ballooning modes. The high ELM frequency of type II ELMs is explained by the facts that the critical pressure gradient defined by the first ballooning stability limit is relatively small and that type II ELMs are very small perturbations which do not cause the pressure gradient to relax very much.

Finally, frame (c) in Fig. 2 corresponds to the highest level of gas puffing in the scan ($\Gamma = 1 \times 10^{23}$ s^{-1}). In this case, magnetic shear is so strong that the operational point never enters the second ballooning stability region. Instead, the operational point is located in the $n = \infty$ ideal (or even resistive) ballooning unstable region for all magnetic surfaces within the ETB. Stability is unambiguously defined by the first ballooning stability limit at $\alpha \lesssim 3.5$ everywhere within the ETB. In this case, violation of the first ballooning stability limit is interpreted to result in type III ELMs (or possibly something resembling poor quality type I ELMs in some cases) and the situation shown in frame (c) in Fig.2 is, consequently, referred to as a type III ELMy H-mode. It should be noted that here the difference between type II and type III ELMs is defined as follows: Type II ELMs occur when the first ballooning stability limit is violated only at the outermost edge, whereas this limit is exceeded in the whole ETB or a significant part thereof for type III ELMs. As will be shown later, this definition is justified, because it allows the model to reproduce the experimental observation that type II ELMs do not cause a significant deterioration of plasma confinement, whereas type III ELMs do.

The present model, even in its ideal formulation, can explain some of the most important characteristics of type III ELMy H-mode, such as the increase in ELM frequency and deterioration of plasma confinement with respect to type I ELMy H-mode, and thereby provide an explanation for many experimental situations with type III ELMs. It is worth noting that in many experiments type III ELMs are characterized by an ELM frequency that decreases with power [1], which is a feature that the ad hoc model used here cannot in itself easily reproduce in ideal MHD. Nevertheless, the model can be extended so that the first ballooning stability boundary is controlled by resistive rather than ideal ballooning modes, which can be the case in highly collisional plasma [23]. This could further reduce the achievable level of the critical pressure gradient below at the first ballooning stability limit.

5. SIMULATION MODEL FOR ELMS

Based on the model described in the preceding section, a new implementation for dynamic modelling of mixed type I-II ELMy H-mode has been included in the JETTO transport code. It is assumed that the ELMs are driven by ballooning modes controlled mainly by the edge pressure gradient. An ELM is triggered when the critical pressure gradient de-fined by an MHD stability limit is exceeded. To a certain extent, the model still implicitly takes into account also the edge current a mechanism controlling the ELMs, since finite n ballooning modes are to some extent driven also by the current and this is taken into account when the stability limits are determined using the MISHKA code.

Figure 3 shows a schematic illustration of the implementation of the ELM model. As discussed in the preceding section, a mixed type I-II ELMy H-mode requires separate stability limits for the outermost and the inner region of the ETB. In accordance with this, the ETB has been divided into two regions in the implementation of the ELM model. In the inner region, the critical pressure gradient is set at a value $\alpha_{c,I}$ defined by the finite n ballooning stability limit, typically $\alpha_{c,I} \approx 6$ whereas in the outer region it is set at a value $\alpha_{c,II}$ defined by the first ballooning stability limit, typically $\alpha_{c,II} \approx 3$. The location of the boundary between the two regions can be chosen arbitrarily and is typically set at $\rho = 0.99$. When the critical pressure gradient $\alpha_{c,I}$ is exceeded in the inner region of the ETB, an ELM having the characteristics of a type I ELM is triggered. Similarly, the system responds with a perturbation corresponding to a type II ELM, when the critical pressure gradient $\alpha_{c,II}$ is exceeded in the outer region.

In both cases, the ELMs are represented by Gaussian-shaped perturbations added on top of the unperturbed radial profiles of the transport coefficients in the pedestal and its vicinity. The use of Gaussian-shaped ELMs is motivated by the fact that the eigenfunctions of the MHD modes supposed to drive the ELMs have Gaussian shapes in linear theory. With this choice of perturbation profile for the ELMs, the perturbed transport coefficient profile $\chi(r)$,where χ stands for ion or electron thermal conductivity or particle diffusivity and r is the radial co-ordinate, can be written

$$\chi(r) = \chi_0(r) + A \exp\left[-\left(\frac{r - r_0}{\Delta r}\right)\right]. \qquad (2)$$

Here, $\chi_0(r)$ is the unperturbed transport coefficient profile corresponding to an inter-ELM state, A is the amplitude of the Gaussian-shaped perturbation, r_0 is the radial location of the centre of the perturbation and Δr is the characteristic width of the perturbation. The parameters A, r_0 and Δr are typically chosen rather differently in the representations of type I and type II ELMs. The current understanding is that the $n = \infty$ ideal ballooning modes assumed to determine the stability of the outermost edge region are much more localized than the finite n ballooning modes assumed to control stability deeper inside the ETB. Some justification for this will be given in the next section. In the present ELM model, the perturbation in the outer region is, therefore, typically a very narrow Gaussian centred close to the separatrix, whereas the inner region of the ETB uses a wider Gaussian centred a little further toward the top of the ETB. In other words, $\Delta r_I > \Delta r_{II}$ and $r_{0.I} < r_{0,II}$, where

the subscripts I and II on the ELM parameters refer to type I and type II ELMs (or inner and outer ETB region), respectively, and r increases when moving from the plasma centre toward the edge. In order to account for the experimental observation that type I ELMs are much larger events than type II ELMs, expelling much more particles and energy, the perturbation in the inner pedestal region is usually given a much larger amplitude than the perturbation in the outer region, i.e. $A_{\mathrm{I}} >> A_{\mathrm{II}}$, the subscripts again referring to type I and type II ELMs.

Typically, the ELMs are ramped up and down over short time intervals, i.e. the ELM amplitude A varies with time t during the ELMs as follows:

$$A\,(t) = \begin{cases} \frac{A_0}{t_2 - t_1}\,(t - t_1), & t_1 \le t < t_2 \\ A_0, & t_2 \le t \le t_3 \\ \frac{A_0}{t_4 - t_3}\,(t_4 - t), & t_3 < t \le t_4. \end{cases} \tag{3}$$

Here, $t_1 < t_2 < t_3 < t_4$ are times defining the beginning and the end of the ramp-up and ramp-down phases of the ELM and A_0 is the maximum ELM amplitude. The total ELM duration $t_{ELM} = t_4 - t_1$ is typically around 1 ms and the flat top phase $t_2 \le \mathrm{t} \le t_3$ about half of that. Different maximum amplitudes $A\chi_i\,(t)$, $A\chi_e\,(t)$ and $A_D(t)$ can be defined for ion thermal conductivity, electron thermal conductivity and particle diffusivity. Usually, the amplification factor for the particle diffusivity is smaller than those for the thermal conductivities.

As outlined in this section, the implementation of the ELM model for mixed type I-II ELMy H-mode features a large number of arbitrary free parameters. In simulations, these parameters are generally chosen in such a way that the individual ELMs remove the right amount of heat and particles consistent with experiments and so that the ELM frequency corresponds to experimental observations.

6. TYPE II ELM WIDTH

In the ELM model for mixed type I-II ELMy H-mode, the type II ELMs are assumed to be controlled by very edge-localized $n = \infty$ ballooning modes. The understanding that the $n = \infty$ ballooning modes limiting stability near the very edge are more localized for strong magnetic shear than the finite n ballooning modes determining stability closer to the top of the ETB can be analytically justified as follows. Reference [24] gives an expression for the width W of the envelope of coupled harmonics forming a ballooning mode eigenfunction in the high n limit with the maximum pressure gradient at the plasma edge:

$$\mathrm{W}\,(x) = \exp\left[-\frac{1}{2}\,|\nu'(\theta_0)|\left(\frac{\partial^2\omega^2}{\partial\psi^2}\Big/\frac{\partial^2\omega^2}{\partial\theta_0^2}\right)^{1/2} x^2\right]. \tag{4}$$

Here, $|\nu'(\theta_0)| = \mathrm{d}q/\mathrm{d}\psi| = |\mathrm{d}'|$ is the derivative of the safety factor with respect to the poloidal flux co-ordinate ψ, ω^2 is the local oscillation frequency of an individual harmonic, θ_0 is the poloidal location of the instability and $x = n^{1/2}\,(\psi - \psi_0)$,where ψ_0 is the location of the minimum of ω^2 in terms of the poloidal flux co-ordinate. Assuming that $\partial^2\,\omega^2\,/\,\partial{\theta_0}^2 \sim \omega^2$ and $\partial^2\,\omega^2/\partial\psi^2 \sim \omega^2/(\Delta\psi_{\mathrm{ETB}})^2$,where $\Delta\psi_{\mathrm{ETB}}$ is the pedestal width, the envelope width can be written as

$$W(\psi) = \exp\left[-\frac{1}{2}\frac{nq'}{\Delta\psi_{ETB}}(\psi-\psi_0)^2\right]. \quad (5)$$

The width of the envelope $\Delta\psi_{envelope}$ thus scales as

$$\Delta\psi_{envelope} \sim \sqrt{\frac{\Delta\psi_{ETB}}{nq'}}. \quad (6)$$

This shows that ballooning modes become very localized in the high *n* limit and for strong magnetic shear at the edge. It should be noted that a $\Delta\psi_{envelope} \sim (nqs)^{-2/3}\, a$ scaling, where *a* is the minor radius at the separatrix, has also been proposed for edge ballooning modes [19]. Recent numerical work, however, suggests a $\Delta\psi_{envelope} \sim (nqs)^{-1/4}\, a$ scaling for low and medium n ballooning modes, which means that these modes usually occupy the whole pedestal [25].

Numerically, the localization and width of high *n* ballooning modes has been studied using the finite *n* ballooning and peeling / kink mode stability code MISHKA. It has been determined how the mode width varies when the inner part of the pedestal is second ballooning stable and the outer part infinite *n* ballooning unstable and the widths of these two regions are changed. The analysis shows that ballooning modes become very narrow and edge localized in the high *n* limit, if a significant part of the pedestal is second ballooning stable and only the outermost edge is infinite n ballooning unstable. Figure 4 illustrates the result for $n = 40$. By perturbing the edge current, the part of the pedestal being second ballooning stable has been varied. Frame (a) shows the eigenfunction for a situation in which the edge current is half of that in the original unperturbed equilibrium. This makes the edge infinite n ballooning unstable from $\psi = 0.935$ to $\psi = 1.000$. The width of the eigenfunction is comparable to the width of the pedestal. In frame (b), the edge current is 1.5 times higher than in the original unperturbed equilibrium. Here, the pedestal is infinite n ballooning unstable only from $\psi = 0.990$ to $\psi = 1.000$. In this case, the eigen-function is almost as narrow as the unstable region and centred close to the edge of the plasma. It should be noted that Saarelma et al. report similar edge localization for low-*n* peeling-ballooning modes in situations with type II ELMs in ASDEX Upgrade [26].

7. RESULTS OF JETTO MODELLING

7.1 DETERMINATION OF OPTIMAL TYPE II ELM WIDTH

In order to test the ELM model for mixed type I-II ELMy H-mode, simulations making use of the MISHKA results shown in Fig.4 were performed. To be specific, a series of simulations was set up corresponding to a series of situations with a wider inner part of the pedestal second ballooning stable and the narrower edge part of it $n = \infty$ ballooning unstable. In these simulations, a Gaussian-shaped perturbation to transport with a char-acteristic width of 4.0cm centred at $\rho = 0965$ was used in the inner region of the ETB. With this choice of parameters, the perturbation representing a type I ELM resembles the eigenfunction in frame (a) in Fig. 4, as far as width and localization are considered. The inner region of the ETB extended from the top of the ETB at around $\rho = 094$ to $\rho = 098$ and the outer

region from $\rho = 0.98$ to the separatrix. Here, the extent of the outer region corresponds roughly to the localization of the eigenfunction in frame (b) in Fig.4 for a high n ballooning mode in a situation with only the outer edge of the pedestal unstable against $n = \infty$ ballooning modes. The ELM perturbation in the outer region was a Gaussian centred at $\rho = 0.995$ and its width was varied. The stability limits were $\alpha_{c,I} = 6.5$ in the inner region of the ETB and $\alpha_{c,II} = 2{:}5$ in the outer region. These values correspond roughly to the finite n ballooning stability limit and the first stability limit, respectively. During the ELMs, ion and electron thermal conductivity was enhanced to a maximum level of 100 $m^2\ s^{-1}$ and 100 $m^2\ s^{-1}$ in the inner and outer regions of the ETB, respectively, reflecting the fact that type II ELMs are tiny compared with type I ELMs. These levels of transport can be compared with the level of thermal neo-classical transport, which is of the order of 0.2 $m^2\ s^{-1}$. Both the type I and the type II ELMs were characterized by a rise time of 0.25ms, a flat top time of 0.5ms and a fall time of 0.25ms, yielding a total ELM duration of 1ms. With this choice of parameters, each type I ELM removes an appropriate amount of plasma thermal energy, about 7% of the total energy content.

For comparison, a reference simulation of pure type I ELMy H-mode was performed with the ELM representation resembling the eigenfunction in frame (a) in Fig.4. In this simulation, the ETB was not split into two regions and, accordingly, a single critical pressure gradient $\alpha_c = 6.5$ was used, corresponding to the finite n ballooning stability limit. The ELMs were represented by a single 4.0 cm wide Gaussian-shaped perturbation centred at $\rho = 0.97$ with the thermal conductivities amplified to a maximum level of 100 $m^2\ s^{-1}$.

In the simulations with mixed type I-II ELMs, the characteristic width of the Gaussian-shaped for the perturbation in the outer pedestal region representing type II ELMs was varied from 1.0cm to 3.0cm in steps of 0.5cm. It should be noted that the width of the perturbation itself varied considerably less than this, because the Gaussian was centred close to the separatrix. Figure 5, which contains time traces of the ion thermal conductivity at $\rho = 0.99$ for each of these cases, shows how the frequencies of type I and type II ELMs are affected by the variation in the width of the type II ELMs. Showing characteristic time traces with frequent small-amplitude type II ELMs interrupted by occasional large-amplitude type I ELMs, the first few frames in the figure indicate that the new ELM model can reproduce the dynamics of mixed type I-II ELMy H-mode with an appropriate choice of simulation parameters. The type II ELM frequency decreases with increasing width of the perturbations representing type II ELMs, because it takes a longer time for the edge pressure gradient to recover from stronger perturbations, which cause a more significant depletion of the pedestal. Wide type II ELMs tend to flatten the pressure profile even inside the outer pedestal region, so that the part of the pedestal with a steeper pressure gradient becomes narrower, prolonging the time it takes for the pressure gradient to build up sufficiently high again in the outer region. Nevertheless, the type I ELM frequency increases with increasing width of the type II ELMs, because the number of type II ELMs between each type I ELM decreases rapidly with the strength of the type II ELMs, whereby the total amount of energy removed between two consecutive type I

ELMs decreases and the pressure gradient can build up to a type I ELM more quickly in the inner region of the pedestal.

It should be noted that the short ELM-free periods after type I ELM crashes before the onset of type II ELMs is a feature seen in some experimental discharges. In simulations with the present ELM model, simulation parameters such as the type II ELM amplitude determine whether this feature is present or not. In the next subsection, an example with a smaller type II ELM amplitude resulting in an almost immediate onset of type II ELMs is shown.

Figure 6 shows time traces of the thermal energy content of the plasma for the simulations with different type II ELM widths. The thermal energy content, and thereby confinement, decreases with increasing type II ELM width. The explanation for this is again that the type II ELMs tend to flatten the pressure profile at the very edge, so that the pedestal effectively shrinks, whereby the pressure at the top of the pedestal drops and the energy stored in the pedestal decreases. Due to profile stiffness this translates into lower core temperatures and thus a smaller total energy content. For comparison, the energy content in the earlier described reference simulation of pure type I ELMy H-mode has also been plotted in Fig.6.

With a type II ELM width of 1.0 cm, the thermal energy content of mixed type I-II ELMy H-mode is only about 15% lower than in the reference simulation of pure type I ELMy H-mode, as is often the case in experiments. With a type II ELM width of 1.5cm, the deterioration of confinement with respect to type I ELMy H-mode is still consistent with that expected for a mixed type I-II ELMy H-mode. If the type II ELM width is 2.0cm or more, the drop in confinement with respect to type I ELMy H-mode is already quite large for a mixed type I-II ELMy H-mode. Moreover, as Fig.5 shows, the number of type II ELMs between each type I ELM becomes unrealistically low for type II ELM widths above 1.5cm. Hence, it can be concluded that the best results for mixed type I-II ELMy H-mode are obtained when the edge-localized perturbations representing type II ELMs have a width of approximately 1.5cm or less. With this choice of type II ELM width and the perturbations centred at $\rho = 0.995$, the radial structure and localization of the type II ELMs closely match the eigenfunction in frame (b) in Fig.4. In conclusion, ballooning modes become very edge localized in the high n limit, if the very edge of the pedestal is infinite n ballooning unstable and the rest of it second ballooning stable, and the dynamics of mixed type I-II ELMy H-mode is best reproduced, when the simulation model corresponds to this situation.

7.2 COMPARISON OF MIXED TYPE I-II ELMY H-MODE WITH OTHER TYPES OF ELMY H-MODE

As shown in the previous subsection, the simulation model described in Sec.5 can reproduce the experimental dynamics of mixed type I-II ELMy H-mode. Here, this is further demonstrated by comparing a simulation of mixed type I-II ELMy H-mode with reference simulations for pure type I, type II and type III ELMy H-mode.

Figure 7 illustrates the ELM behaviour in a typical simulation of mixed type I-II ELMy H-

mode, which will be compared with the reference simulations for other types of ELMy H-mode. Frame (a) in Fig.7 shows the ion thermal conductivity at the magnetic surface $\rho = 0.995$ as a function of time, featuring the characteristic experimentally observed behaviour for mixed type I-II ELMy H-mode with quasi-continuous small-amplitude type II ELMs interrupted by occasional large-amplitude type I ELMs. The simulation was performed with a high edge density defined by the boundary condition $n_0 = 3.33\times10^{19}\mathrm{m}^{-3}$ at the separatrix, which is typical for mixed type I-II ELMy H-mode. Consistent with the high edge density, the boundary conditions for the temperature at the separatrix were a modest $T_0 = 30\mathrm{eV}$ for both ions and electrons and a high neutral beam heating power of $P = 16\mathrm{MW}$ was applied. The self-consistency of the boundary conditions in similar simulations has been studied in previous work on integrated modelling [13]. The critical pressure gradient had the values $\alpha_{c,I} = 6.0$ and $\alpha_{c,II} = 3.0$, typical for mixed type I-II ELMy H-mode, in the inner and outer regions of the ETB, respectively. Ion and electron thermal conductivity during the ELMs was amplified to a maximum of $50\mathrm{m}^2\,\mathrm{s}^{-1}$ and $2\mathrm{m}^2\,\mathrm{s}^{-1}$, in the inner and outer regions of the ETB, respectively, corresponding to increases of roughly 250 and 10 times the level of thermal neo-classical transport. The diffusion coefficients were enhanced considerably less during the ELMs, to a maximum of 25 and 3 times the initial neo-classical level, in the inner and outer regions of the ETB, respectively. Again, the ELM perturbations were Gaussians with characteristic widths of 4.0cm and 1.0cm centred at $\rho = 0.965$ and $\rho = 0.995$, in the inner and outer regions, respectively. Both the type I and the type II ELMs were characterized by a rise time of 0.25ms, a flat top time of 0.50ms and a fall time of 0.25ms, yielding a total ELM duration of 1.00ms. Frame (b) in Fig.7 shows the ion thermal conductivity at another flux surface, $\rho = 0.965$, providing together with frame (a) some illustration of the localization of each ELM type. As shown in frame (b), the small type II ELMs do not affect the transport coefficients in the inner region of the ETB at $\rho = 0{:}965$. At this radius, the time trace of the ion thermal conductivity looks like that of a pure type I ELMy H-mode, because the type II ELMs are completely localized further to the edge. It should be noted that the perturbations added to the transport coefficients due to the large type I ELMs are, on the contrary, very significant in the whole pedestal. The relative levels of transport enhancement in the inner and outer pedestal regions can be discerned by comparing frames (a) and (b) in Fig.7.

A reference type I ELMy H-mode simulation was performed using the value $\alpha_c = 6.0$ for the critical pressure gradient, i.e. the same value as for type I ELMs in the simulation of mixed type I-II ELMy H-mode, corresponding to the finite n ballooning stability limit. Transport during the ELMs was enhanced using a single Gaussian-shaped perturbation having the same amplitude, e.g. amplification factor about 250 for the thermal conductivities, and the same characteristic width, 4cm, as the Gaussian-shaped perturbation for type I ELMs in the reference simulation of mixed type I-II ELMy H-mode. The ELM perturbation in the simulation of pure type I ELMy H-mode was centred at $\alpha = 0.97$, i.e. slightly closer to the edge than in the simulation of mixed type I-II ELMy H-mode, in order to cover the edge properly. The lengths of the rise, top and fall phases of the ELMs were kept the same as before, yielding a total ELM duration of 1 ms. The simulation was

performed at a lower density than the simulation of mixed type I-II ELMy H-mode in order to reflect the fact that type I ELMy H-mode generally occurs in lower density ranges than mixed type I-II ELMy H-mode in experiments. Specifically, the separatrix density boundary condition was a modest $n_0 = 5\times10^{18}$ m^{-3}. The separatrix temperature boundary conditions were raised to $T_0 = 200$eV for both electrons and ions in order to keep the same pressure at the separatrix as in the simulation of mixed type I-II ELMy H-mode. The neutral beam heating power was P = 16 MW, i.e. the same as in the simulation of mixed type I-II ELMy H-mode, the high value being characteristic for the type I ELMy H-mode regime.

Similarly, a reference run for type III ELMy H-mode was set up using $\alpha_c = 3.0$ for the critical pressure gradient and a 4.0 cm wide Gaussian-shaped perturbation centred at $\rho = 0.97$ in order to cover the whole ETB properly. The ELM amplitude was set to correspond to the type II ELM amplitude in the reference simulation of mixed type I-II ELMy H-mode, so that e.g. the thermal conductivities were amplified to $2m^2s^{-1}$ during the ELMs. The durations of the ELM phases were the same as in the simulation of mixed type I-II ELMy H-mode, i.e. the total ELM duration was 1 ms. With this choice of ELM amplitude and ELM duration, the simulated type III ELMs remove an amount of plasma energy consistent with experimental observations. In order to reflect the fact that type III ELMy H-mode experimentally occurs in even higher density ranges than mixed type I-II
ELMy H-mode, the separatrix density boundary condition was raised to the high level of $n_0 = 5\times10^{18}$ m^{-3}. The separatrix temperature boundary conditions were set at a modest $T_0 = 20$eV for both electrons and ions in order to keep the pressure at the separatrix the same as in the other simulations. The neutral beam heating power was kept at the high level of P = 16MW, which is still reasonable for type III ELMy H-mode, since the density is high. JET Pulse No: 52739 used in Fig.1 with P = 14.4MW neutral beam heating power is an example of such a high-power type III ELMy H-mode. At lower densities, the high level of heating power would correspond to the type I ELMy H-mode regime.

Finally, a reference simulation of pure type II ELMy H-mode was run using $\alpha_c = 3.0$ for the critical pressure gradient and a Gaussian with a characteristic width of 1.0cm centred at $\rho = 0.995$ as ELM perturbation. The ELM amplitude was the same as for the type II ELMs in the reference simulation of mixed type I-II ELMy H-mode, i.e. the thermal conductivities were enhanced to $2m^2s^{-1}$. To put it simply, the type II ELM representation was taken unchanged from the mixed type I-II ELMy H-mode simulation and the type I ELM representation was omitted completely. As in the simulation of mixed type I-II ELMy H-mode, the separatrix density boundary condition was $n_0 = 3.33\times10^{19}$ m^{-3} and the separatrix temperature boundary conditions $T_0 = 30$eV for both electrons and ions. The neutral beam heating power was reduced to P = 8MW in order to limit the pressure gradient in the inner part of the ETB to a physically meaningful level. Without reducing
the power, the pressure gradient in the inner part of the pedestal, where no critical pressure gradient limit is applied, would rise to unphysical levels higher than in pure type I and mixed type I-II ELMy H-mode.

Figure 8 compares the ELM characteristics of the simulations of mixed type I-II, type I, type II

and type III ELMy H-mode shown in frames (a), (b), (c) and (d), respectively. The plots are time traces of the ion thermal conductivity. It should be noted that the frequency of type I ELMs in the simulation of mixed type I-II ELMy H-mode is lower than the ELM frequency in the simulation of pure type I ELMy H-mode, which is consistent with experimental observations. The lower type I ELM frequency in mixed type I-II ELMy H-mode can be attributed mainly to two causes. For one thing, the energy and particle losses associated with the type II ELM activity between the type I ELMs increase the time it takes for the pressure gradient to recover from a type I ELM crash. Secondly, the higher edge density in the simulation of mixed type I-II ELMy H-mode results in greater neo-classical losses between the ELMs, which also increases the ELM recovery time.

Figure 9 shows time traces of the thermal energy content (shown in frame (a)) and the confinement factor H98Y (shown in frame (b)) for the four reference simulations of different types of ELMy H-mode. It is of interest to compare the relative levels of the thermal energy content and the confinement factor for the different types of ELMy H-mode. Pure type I ELMy H-mode is generally characterized by high thermal energy content and high confinement, as in Fig. 9. The simulation of mixed type I-II ELMy H-mode, however, has only 3% lower pre-ELM thermal energy content than the reference simulation of pure type I ELMy H-mode. Measured in terms of confinement factor H98Y, the difference between the simulations is greater, about 20%. The result is consistent with the experimental observation that pure type I ELMy H-mode often has slightly better plasma performance than mixed type I-II ELMy H-mode. In the simulation of type III ELMy H-mode, which as in experiments has the lowest level of confinement, the thermal energy content measured just before ELMs is about 26% lower than in the simulation of pure type I ELMy H-mode. The difference is of the order of 37% in terms of confinement factor H98Y. The simulation of pure type II ELMy H-mode has higher confinement than the simulation of type III ELMy H-mode, but slightly lower confinement than the simulation of mixed type I-II ELMy H-mode. The thermal energy content in the simulation with pure type II ELMs is about 23% lower than the pre-ELM thermal energy content in the simulation of pure type I ELMy H-mode. The difference is about 25% measured in terms of confinement factor H98Y. Since pure type II ELMy H-mode has never been achieved at JET, the
results obtained for this type of operation are difficult to verify.

In the simulation of pure type I ELMy H-mode with strong ELMs, each ELM removes about 9.5% of the plasma energy. In the simulation of mixed type I-II ELMy H-mode, the relative energy loss during the type I ELMs is slightly smaller as a result of the different density and temperature profiles. The type II ELMs, both in the simulation of mixed type I-II ELMy H-mode and in the simulation of pure type II ELMy H-mode remove only of the order of 0.1% of the plasma energy content per ELM. However, since the type II ELMs are very frequent, this is still enough to have a non-negligible influence on the recovery time between the type I ELMs in the simulation of mixed type I-II ELMy H-mode. Finally, in the simulation of type III ELMy H-mode, the ELMs remove of the order of 1% of the total energy content per ELM, which distinguishes them from the type II ELMs.
The different levels of thermal energy content and confinement in the simulations are a result of

how the different ELM types shape the pedestal pressure profile. Due to profile stiffness, the temperature at the top of the pedestal determines the temperature level also in the core. Because the total plasma thermal energy content is proportional to the integral over the pressure profile, the pedestal pressure profile thus effectively determines the level of total energy content. Figure 10 shows the pedestal pressure profiles in the simulations of type I, mixed type I-II, type II and type III ELMy H-mode. In the case of type I and mixed type I-II ELMy H-mode, the times used in the plot correspond to pre-type I ELM states, at which the pressure gradient has reached its maximum. Type I ELMy H-mode has the highest pressure at the top of the pedestal and the highest level of energy stored in the pedestal. The pedestal pressure gradient corresponds to $\alpha_c = 6.0$ specified for the simulation. In the simulation of mixed type I-II ELMy H-mode, the same level of pressure gradient is achieved in the inner region of the ETB. However, the pressure gradient in the outer region of the ETB is much flatter due to the condition $\alpha_{c,II} = 3.0$ set for the type II ELMs, which effectively causes the pedestal to shrink with respect to type I ELMy H-mode. Because of this, the pressure achieved at the top of the pedestal is lower than in type I ELMy H-mode. In the case of pure type II ELMy H-mode, the pressure profile in the region next to the separatrix is determined by the critical pressure gradient $\alpha_c = 3.0$ and corresponds roughly to the pressure profile in the outer region of the ETB in the case of mixed type I-II ELMy H-mode. Further inside the separatrix, no critical pressure gradient has been applied, whereby the pressure gradient has freely evolved to a steady state level characteristic of the system. By increasing the heating power, the pressure gradient in this inner part of the ETB can be made steeper, leading to an increased total energy content. Hence, the level of thermal energy content for pure type II ELMy H-mode in Fig.9 could easily be increased almost to the level achieved with mixed type I-II ELMy H-mode. As noted earlier, it is not very physical to let the pressure gradient in the inner region of the pedestal become steeper than in mixed type I-II ELMy H-mode, hence the reduced level of heating power in the simulation of pure type II ELMy H-mode. In the case of type III ELMy H-mode, the pressure gradient is limited by the low limit $\alpha_{cI} = 3.0$ in the whole pedestal, which translates into a low level of pressure at the top of the pedestal. This explains the low level of confinement in type III ELMy H-mode.

7.3 MHD STABILITY

According to the model presented in Sec.4, type I ELMy H-mode corresponds to a situation in which the discharge stays in the second ballooning stability region for all magnetic surfaces within the ETB. Similarly, mixed type I-II ELMy H-mode is proposed to be a situation with most of the pedestal second ballooning stable, but the very edge infinite *n* ballooning unstable. Here, MHD stability analysis performed on interpretative transport simulations is used to demonstrate that the model is in agreement with actual experimental situations. In interpretative simulations, the density and temperature profiles are taken from experimental data, whereas the evolution of the current is predicted. MHD stability analysis is carried out when the simulation has reached a good steady state.

Here, JET Pulse No: 55973 with type I ELMs is compared in terms of MHD stability with JET

Pulse No: 56044, which has mixed type I-II ELMs. The difference in the ELM characteristics of the two discharges is a result of their rather different experimental parameters. To be specific, discharges 55973 and 56044 have different toroidal magnetic fields, $B_0 = 2.40$T and $B_0 = 2.66$T, respectively, on the axis, different plasma currents, I = 2.0MAand I = 2.5MA, respectively, different levels of external neutral gas fuelling, $\Gamma = 0$ and $\Gamma = 5 \times 10^{22}$ s^{-1}, respectively, and slightly different levels of heating power, P = 10MW and P = 11.5MW, respectively, by neutral beam injection. Edge and core Lidar (Thomson scattering) data for both temperature and density and electron cyclotron emission spectroscopy and charge exchange recombination spectroscopy data for the temperature have been used in the interpretative JETTO simulations. MHD sta-bility analysis of the interpretative runs shows that discharge 55973 with type I ELMs is second ballooning stable for all magnetic surfaces within the ETB. Ballooning stability is uniquely determined by the finite n ballooning stability limit. In the case of discharge 56044, most of the pedestal is second ballooning stable, but the edge outside $\rho = 0.983$ is infinite n ballooning unstable. This is illustrated in Fig.11, which compares MHD stability diagrams for the magnetic surface $\rho = 0.99$ for the interpretative simulations of the two discharges. The figure contains two stability diagrams in -s space with the mode numbers of the most unstable kink, peeling or ballooning modes ($n \leq 14$) and the $n = \infty$ ballooning unstable region indicated. This result obtained with MHD stability analysis performed directly on interpretative modelling using experimental profiles adds validity to the model for mixed type I-II ELMy H-mode.

It should be noted that an ideal MHD version of the MISHKA code was used to calculate the results shown in Fig.11. In non-ideal MHD, some of the ideal MHD modes with low growth rates given by the code might be stabilized by the finite gyro radius effect of the ion diamagnetic drift frequency ω_i. Therefore, modes with growth rates lower than or equal to

$$\omega_{i*} = \frac{m}{r} \frac{T_i}{e_i B_0} \frac{d \ln p_i}{dr} \tag{7}$$

have been excluded from the plots in Fig.11. Here, m is the poloidal mode number, r is the local minor radius, T_i is the ion temperature, ei is the ion charge, B_0 is the toroidal magnetic field on the magnetic axis and pi is the ion pressure. The ion diamagnetic drift frequency has been evaluated at the radius of largest amplitude of the MHD modes, where the instabilities can be assumed to be strongest.

8. EFFECT OF THE MAGNETIC CONFIGURATION ON THE OCCURRENCE OF TYPE II ELMS IN H-MODE PLASMAS

In Sec.2 it was noted that quasi double null magnetic configurations have been experimentally observed at ASDEX Upgrade to be favourable for the occurrence of type II ELMs. Type II ELMs have been observed both with single null and quasi double null magnetic configurations, but quasi double null magnetic configurations seem to ease the occurrence of them. Here, the effect of the magnetic configuration on MHD stability and thus on ELM behaviour has been investigated by

comparing interpretative JETTO simulations with single null and quasi double null configurations.

In a first pair of simulations, JET Pulse No: 53703, with a changing magnetic configu-ration was used in the analysis. In this discharge, the magnetic configuration changes from single null via quasi double null to double null in a few seconds. JETTO was run in the interpretative mode in two separate simulations, one of them with a good single null configuration from discharge 53703 and the other one with a good quasi double null configuration from the same discharge. In order to include only the direct effect of the magnetic configuration on magnetic shear and edge stability and to exclude the indirect effect due to a difference in the plasma profiles resulting from the different magnetic configurations, exactly the same density and temperature profiles where used in both sim-ulations. Figure 12 shows radial profiles of the magnetic shear in both simulations. The effect of the quasi double null configuration is to cause magnetic shear to increase strongly in the pedestal and its immediate vicinity. MHD stability analysis was carried out on the simulations. Despite the stronger magnetic shear in the simulation with the quasi double null magnetic configuration, ballooning stability is not qualitatively different in the two simulations, because the infinite n ballooning stability boundary moves in response to a change in the magnetic configuration. To be specific, both the stability boundary and the operational point are located at higher levels of magnetic shear with the quasi double null configuration than with the single null configuration. The simulations were repeated with several different density profiles, but in each case the distance between the operational point and the infinite n ballooning stability boundary was roughly the same with both configurations. With modest edge densities, both the simulation with the single null magnetic configuration and the one with the quasi double null configuration are second ballooning stable for all magnetic surfaces within the ETB. With higher edge densities, the edge becomes infinite *n* ballooning unstable in both simulations. Therefore, it can be concluded that a quasi double null magnetic configuration does not necessarily in itself directly make the edge more unstable against infinite *n* ballooning modes than a single null magnetic configuration, despite causing an increase in magnetic shear at the edge. Hence, the result indicates that a quasi double null magnetic configuration is not nec-essarily in itself more favourable for the occurrence of type II ELMs than a single null magnetic configuration, according to the present ELM model.

The favourability for type II ELMs attributed to quasi double null configurations seems to be due to the fact that quasi double null magnetic configurations are generally sociated with higher average density than single null configurations. Typically, a quasi double null discharge can have up to 20% higher average density than a single null discharge with similar plasma parameters. As shown in Sec.4, the edge density affects ballooning stability very sensitively. Consequently, the comparison of single null and quasi double null plasmas was repeated using actual experimental density and temperature profiles in interpretative JETTO simulations. JET Pulse No: 56044 with a single null magnetic configuration, already discussed in the previous section, and 56083 with a quasi double null configuration were selected for comparison. Since these two discharges otherwise have very similar plasma parameters, any difference in MHD stability between them should either

directly or indirectly be due to the different magnetic configurations. In particular, the two discharges have the same toroidal magnetic field $B_0 = 2.66$T on the axis, the same plasma current I = 2:5 MA, the same level of external heating power $P = 12$MWby neutral beam injection and the same level of external neutral gas fuelling $\Gamma = 5\times10^{22}$ s^{-1}. The density in the pedestal is higher in discharge 56083 with the quasi double null configuration than in discharge 56044 with the single null configuration by at least 5×10^{18} s^{-3}. The different magnetic configurations seem to be the only reason for the difference in density. The experimental profiles used in the simulations were fits to edge and core Lidar data for both temperature and density and to electron cyclotron emission spectroscopy and charge exchange recombination spectroscopy data for the temperature. Both discharges 56044 and 56083 have mixed type I-II ELMs. It would of course be even more interesting to compare a type I ELMy H-mode discharge with a mixed type I-II ELMy H-mode discharge rather than two discharges with mixed type I-II ELMs, but suitable discharges differing only with respect to the magnetic configuration are not easy to find. The difference between type I and mixed type I-II ELMy H-mode discharges in terms of MHD stability has, however, already been demonstrated in the previous section. The comparison in this section still shows both qualitatively and quantitatively how the quasi double null configuration influences MHD stability in a way favourable for type II ELMs.

The difference in MHD stability between Pulse No's: 56044 and 56083 is seen by comparing the magnetic surface $\rho = 0.98$, for which Fig.13 shows MHD stability diagrams. As before, the mode numbers of the most unstable kink, peeling or ballooning modes ($n \leq 14$) and the $n = \infty$ ballooning unstable region are indicated in the -s space. Again, modes with growth rates lower than or equal to the ion diamagnetic drift frequency have been excluded, because the results were obtained for ideal MHD. Frame (a) shows that the simulation with the single null magnetic configuration is stable against infinite n ballooning modes at the magnetic surface $\rho = 0{:}98$. In the previous section, it was shown that the discharge is infinite n ballooning unstable closer to the edge at $\rho = 0.99$, as expected for a mixed type I-II ELMy H-mode. Frame (b) reveals that the simulation with the quasi double null configuration is unstable against infinite n ballooning modes at $\rho = 0.98$. In conclusion, both discharges are unstable against infinite n ballooning modes at the edge, but the unstable region is slightly wider with the quasi double null magnetic configuration than with the single null magnetic configuration. With the quasi double null magnetic configuration, magnetic shear at the edge is stronger, which makes the edge more unstable against infinite n ballooning modes. Hence, the present model, which explains mixed type II ELMs as a situation with the outermost edge infinite n ballooning unstable, indicates that a quasi double null magnetic configuration can be favourable for the occurrence of type II ELMs. However, the quasi double null magnetic configuration seems to be more favourable for the occurrence of type II ELMs than the single null magnetic configuration primarily because it results in a higher edge (and average) density.

So far, the discussion on the effect of the magnetic configuration on ELM behaviour has been limited to single null and quasi double null magnetic configurations. It is of interest to consider

how a true double null magnetic configuration affects ballooning stability and ELM behaviour. Preliminary modelling indicates that a double null magnetic configuration just quantitatively reinforces the trends obtained when pushing the plasma from a single null to a quasi double null magnetic configuration.

9. EFFECT OF P ON THE OCCURRENCE OF TYPE II ELMS IN H-MODE PLASMAS

As noted in Sec.2, high β_p has been experimentally observed e.g. at JT-60U to be favourable for the occurrence of type II ELMs in H-mode plasmas. The effect of β_p on infinite n ballooning stability has been studied by running HELENA on a series of predictive JETTO simulations with varying β_p. Since the influence of β_p is subtle, it is easier to demonstrate the effect through predictive modelling, which allows suitable cases to be constructed, rather than to try to find discharges differing only with respect to β_p and ELM type. In predictive simulations, different levels of β_p can be obtained e.g. by adding different fractions of suprathermal energy content on top of the thermal energy content in the pressure used when solving the Grad-Shafranov equation in recalculations of the equilibrium with JETTO's equilibrium solver ESCO. Here, the effect of β_p poloidal is demonstrated using two predictive simulations with the nominal pressure multiplied by 1.2 and 2.4, respectively, in the equilibrium recalculations. In the latter simulation, the effective level of p is, consequently, two times higher than in the former one or about $\beta_p = 2.6$ compared to $\beta_p = 1,3$, the values evolving slightly over time. In both cases, the simulations were first run for 0.5s in L-mode, whereupon the plasma was allowed to evolve in H-mode toward a steady state without imposing ELMs on it. The boundary conditions were $n_0 = 2.9\times10^{19}$ m^{-3} for the edge density and $T_0 = 100$eV for the electron and ion edge temperature, and the total plasma current was $I = 2.5$ MA. Infinite n ballooning stability analysis was carried out 1.0s after the transition to H-mode, when the pressure gradient had evolved to a level roughly corresponding to the finite n ballooning stability limit.

Figure 14 shows radial profiles of magnetic shear at the times chosen for MHD stability analysis in the two simulations with low and high β_p. It is evident that magnetic shear within the ETB increases strongly with β_p, which implies that the edge is more unstable in the simulation with high β_p. It should be noted that the width of the ETB increases in terms of the toroidal flux co-ordinate ρ with increasing β_p. This effect is due to the Shafranov shift of the flux surfaces, which increases with increasing β_p. The absolute width of the ETB does not increase, since the magnetic surfaces only become more closely packed at the outer side of the plasma.

The results of infinite n ballooning stability analysis for the low and high β_p simulations are illustrated in Fig.15, which shows $n = \infty$ ballooning stability diagrams with the normalized pressure gradient on the horizontal axis and magnetic shear s on the vertical axis for two different flux surfaces, $\rho = 0.97$ and $\rho = 0.99$. The results have been obtained by running the MHD equlibrium solver HELENA on a series of equilibria with systematically changing perturbations in edge pressure gradient and edge current. The operational point corresponding to the unperturbed equilibrium is

shown for each case. In the simulation with the lower value of β_p, the operational point is located in the second ballooning stability region for both $\rho = 0.97$ and $\rho = 0.99$. In fact, the pedestal is completely second ballooning stable in this case. In the simulation with the higher value of β_p, the situation is qualitatively different. As shown in Fig.15, $\rho = 0.97$ is second ballooning stable, whereas $\rho = 0.99$ is infinite n ballooning unstable. More precisely, the pedestal is unstable from $\rho = 0.988$ to the separatrix. The qualitative difference in $n = \infty$ ballooning stability between the two analyzed simulations with different β_p is due to the fact that magnetic shear at the edge is higher in the simulation with higher β_p. According to the present model, the situation with the lower β_p corresponds to a pure type I ELMy H-mode, whereas the situation with the higher p corresponds to a mixed type I-II ELMy H-mode. Because the predictive simulations analyzed here essentially differ only with respect to β_p, the difference in ballooning stability can be attributed entirely to this parameter and the modelling thus implies that high β_p is favourable for the occurrence of type II ELMs in H-mode plasmas by making the outermost edge of the plasma more unstable against $n = \infty$ ballooning modes.

10. EFFECT OF THE EDGE SAFETY FACTOR ON THE OCCURRENCE OF TYPE II ELMS IN H-MODE PLASMAS

In Sec.2 it was noted that situations with a combination of high edge safety factor q and high triangularity δ have been found to be favourable for type II ELMs in experiments. Here, the effects of the edge safety factor and triangularity are investigated separately, starting with the effect of the edge safety factor in this section. For simplicity, the same approach as in the preceding section discussing the effect of β_p is followed.

To begin with, two predictive JETTO simulations with different q profiles were con-structed by varying the boundary condition for the current. The plasma was allowed to evolve toward a steady state without imposing ELMs on it. Infinite n ballooning stability analysis was carried out when the pressure gradient had a evolved to a level roughly cor-responding to the finite n ballooning stability limit. Figure 16 shows the radial profiles of the total current density in frame (a), of the safety factor in frame (b) and of magnetic shear in frame (c) for two the predictive JETTO simulations with different levels of edge safety factor. The total current was I = 2.1MA and I = 2.5MAin the high and low q simulations, respectively. In both cases, the boundary conditions were $n_0 = 2.5 \times 10^{19}\ m^{-3}$ for the edge density and $T_0 = 100$eV for the electron and ion edge temperature. With these boundary conditions, the safety factor takes the values $q_{95} = 4.25$ and $q_{95} = 3.69$ at $\rho = 0{:}95$ for I = 2.1MAand I = 2.5MArespectively, at the time chosen for ballooning stability analysis, i.e. when the pressure gradient has evolved to a level roughly corresponding to the finite n ballooning stability limit. It is evident that magnetic shear at the edge increases with increasing edge safety factor. Analogously with the analysis in the preceding section, the increase in magnetic shear tends to push the operational point at the outermost magnetic surfaces into the n = 1 ballooning unstable region, i.e. create a situation corresponding to an H-mode with type II ELMs according to the present model.

Figure 17 illustrates the results of $n = \infty$ ballooning stability analysis for the situations with $q_{95} =$

3.69 and $q_{95} = 4.25$. Stability diagrams are again shown for the magnetic surfaces $\rho = 0.97$ and $\rho = 0.99$, as in the preceding section on the effect of β_p. In the case with the lower q, both $\rho = 0.97$ and $\rho = 0.99$ are second ballooning stable flux surfaces. In fact, the operational point stays in the second ballooning stability region for all magnetic surfaces within the ETB, implying that the simulation in terms of infinite n ballooning stability corresponds to a pure type I ELMy H-mode. In the case with the higher q, $\rho = 0.97$ is second ballooning stable, whereas $\rho = 0.99$ is infinite n ballooning unstable. To be specific, the pedestal is infinite n ballooning unstable from $\rho = 0.985$ to the separatrix. According to the model used in this paper, the simulation with higher q corresponds to a plasma with type II ELMs. Hence, the overall result from the simulationsunder consideration is that high q at the edge seems to be favourable for the occurrence of type II ELMs.

11 EFFECT OF TRIANGULARITY ON THE OCCURRENCE OF TYPE II ELMS IN H-MODE PLASMAS

In this section, the effect of triangularity on the ELM characteristics is examined separately, in the same way as the effect of the edge safety factor was examined in the preceding section. Using a momentum approximation for an up-down symmetric plasma boundary, three predictive JETTO simulations with triangularities $\delta = 0.3$, $\delta = 0.4$ and $\delta = 0.5$ have been performed. By changing the minor radius slightly, the plasma volume was kept the same in all three cases. Since changing the minor radius affects the q profile, the boundary condition for the total current was also slightly different in each case in order to keep the level of the edge safety factor constant. The separatrix density was $n_0 = 2.3\times10^{19}m^{-3}$ and the ion and electron temperatures at the separatrix $T_0 = 100$eV in each of the cases. Figure 18 shows the radial profiles of magnetic shear in the three simulations. As expected, magnetic shear at the edge increases with increasing triangularity. Infinite n ballooning stability analysis was performed on the simulations. It turns out that all three simulations are qualitatively very similar with respect to infinite n ballooning stability, despite the increase in magnetic shear with triangularity. The explanation for this is that the stability boundary evolves strongly as a function of the triangularity. Due to this effect, the simulations do not become more infinite n ballooning unstable at the edge with increasing triangularity. This result could imply that the edge safety factor might be more important than triangularity for obtaining plasma conditions favourable for the occurrence of type II ELMs. Since high triangularity clearly provides the necessary increase in magnetic shear very efficiently, it is understandable that this feature still seems to be beneficial for operation with type II ELMs. However, there is a more plausible explanation for the result obtained in this section: An increase in triangularity usually leads to an increase in edge density, in the same way as a transition from a single null to a quasi double magnetic configuration, and this has been shown to affect ballooning stability sensitively. The effect on the density is not taken into account in the predictive simulations. Taking into account the density increase associated with high triangularity, it becomes straightforward to show that increasing triangularity makes the edge more unstable against infinite n ballooning modes, which according to the present model

shows high triangularity to be favourable for the occurrence of type II ELMs. This result would also be consistent with the experimental observation that both the edge safety factor and the triangularity influence the occurrence of type II ELMs.

SUMMARY AND DISCUSSION

Being characterized by rather good confinement properties and small, benign ELMs producing only modest heat loads on the divertor plates, mixed type I-II ELMy H-mode offers a promising mode of operation for future tokamak plasmas. Experimentally, mixed type I-II ELMy H-mode has been observed in a number of situations: in discharges with relatively strong external neutral gas puffing, with quasi double null magnetic configurations, with high p and with high edge safety factor and high triangularity.

Using predictive transport simulations with different levels of external neutral gas puffing as examples, a simple model based on $n = \infty$ ideal ballooning and finite n ballooning / peeling mode stability for different ELM types has been presented. Type I ELMs are proposed to be caused by violations of the finite n ballooning stability limit, whereas type II ELMs are suggested to occur when infinite n ideal ballooning stability is violated at the very edge of the plasma. Type III ELMs are proposed to occur when infinite n ideal ballooning stability is violated in a region, the width of which is comparable to the width of the whole ETB. In the case of a highly collisional plasma, ballooning stability can be controlled by resistive rather than ideal modes. Qualitatively, the model explains the experimentally observed transition from type I to type III ELMs and the accompanying increase in ELM frequency and deterioration of plasma confinement as a transition from second to first ballooning stability. The model provides possible explanations for many of the characteristics of various types of ELMy H-mode, in particular for the increasing ELM frequency in type I ELMy H-mode with power, for the modest deterioration of plasma confinement in mixed type I-II ELMy H-mode with respect to pure type I ELMy H-mode and for the significant deterioration of confinement in type III ELMy H-mode with respect to type I ELMy H-mode as well as for the high ELM frequencies in type II and III ELMy H-mode.

As shown in this paper, it is possible to reproduce the experimental dynamics of the most important types of ELMy H-mode using an appropriate implementation of the proposed model. Here, mixed type I-II ELMy H-mode has been modelled using the JETTO transport code with the ETB divided into an inner and an outer region, in which stability for type I and type II ELMs, respectively, is evaluated using appropriate limits for the pressure gradient derived from MHD stability analysis. The ELMs are represented by Gaussian-shaped perturbations to the radial profiles of the transport coefficients. Some justification from theory and numerical analysis has been given for the characteristics of the ELMs. Type I, pure type II and type III ELMy H-modes have been modelled with a simpler scheme using just a single critical pressure gradient and a single type of perturbations. The ELM model also provides a plausible way to explain why some special effects and situations such as strong gas puffing, a quasi double null magnetic configuration, high β_p and high edge

safety factor and high triangularity can be favourable for type II ELMs. By performing MHD stability analysis on interpretative and predictive JETTO simulations, it has been shown that these situations lead to a strong increase in magnetic shear at the very edge of the plasma, which can cause this outermost region to become infinite n ballooning unstable, thereby effectively returning the operational point back to the first stability region.

A general observation in this study is that the operational range for type II ELMs is rather narrow in terms of e.g. density, power, poloidal β and edge safety factor, which is consistent with experiments. For instance, a slight increase in density, or equivalently a slight decrease in power, causes a mixed type I-II ELMy H-mode to transfer into a type III ELMy H-mode. Infinite n ballooning stability analysis performed on the different scenarios discussed in this paper indicates that the edge density, which can be controlled by e.g. external gas puffing, is the most important parameter controlling the transitions between different types of ELMy H-mode. Parameters such as p and the edge safety factor clearly play a role in determining the ELM type, but only in limited density ranges. In many of the examples used in this paper, the edge density has deliberately been chosen so that other effects become apparent.

The modelling does not unambiguously show quasi double null magnetic configurations and high triangularity in themselves to be effects favourable for type II ELMs. Nevertheless, it is shown that quasi double null magnetic configurations and high triangularity lead to a strong increase in magnetic shear at the edge. In the predictive simulations, which do not take into account the effect of the magnetic configuration and plasma shaping on the density profile, the operational point does not become more unstable despite the strong increase in magnetic shear, because the $n = \infty$ ballooning unstable region shrinks sig-nificantly with the increasing magnetic shear. Quasi double null magnetic configurations and high triangularity seem to be more favourable for the occurrence of type II ELMs primarily because they result in a higher edge (and average) density than single null magnetic configurations and low triangularity, respectively. As mentioned in the paper, type II ELMs have been experimentally observed (among other situations) for combinations of high edge safety factor and high triangularity. The result obtained here could also indicate that the edge safety factor might be more important than the triangularity as far as favourability for type II ELMs is concerned.

ACKNOWLEDGEMENTS

This work has been performed under the European Fusion Development Agreement.

REFERENCES

[1]. A.V. Chankin, G. Saibene, Plasma Phys. Control. Fusion 41 913 (1999).

[2]. J.W. Connor, Plasma Phys. Control. Fusion 40 531 (1997).

[3]. W. Suttrop, Plasma Phys. Control. Fusion 42 A1 (1999).

[4]. ITER Physics Experts Groups on Confinement and Confinement and Transport Modelling and Database, ITER Physics Basis Editors, ITER EDA, Nucl. Fusion 39 2175 (1999).

[5]. G. Saibene et al., Proc. 28th EPS Conference on Plasma Physics and Controlled Fusion, Madeira, Portugal, 18-22 June 2001.
[6]. Y. Kamada et al. Plasma Phys. Control. Fusion 44 A279 (2002).
[7]. Y. Kamada et al., Plasma Phys. Control. Fusion 42 A247 (2000).
[8]. L. Lao et al. Nucl. Fusion 41 295 (2001).
[9]. J. Stober et al. Nucl. Fusion 41 1123 (2001).
[10]. O. Gruber et al., Proc. 19th IAEA Conference, Lyon, France (2002).
[11]. G. Cennachi, A. Taroni, JET-IR(88)03 (1988).
[12]. A.B. Mikhailovskii et al.,PlasmaPhys.Rep.23 844 (1997).
[13]. J.-S. Lönnroth et al., Plasma Phys. Control. Fusion 45 1689 (2003).
[14]. M. Erba et al., Plasma Phys. Controlled Fusion 39 261 (1997).
[15]. W.A. Houlberg, K.C. Shaing, S.P. Hirshman, M.C. Zarnstorff, Phys. Plasmas 4 3231 (1997).
[16]. T. Onjun, A. Kritz, G. Bateman, V. Parail, J. Lönnroth, G. Huysmans, submitted to Phys. Plasmas (2003).
[17]. T. Onjun, G. Bateman, A.H. Kritz, G. Hammet, Phys. Plasmas 9 5018 (2002).
[18]. G.T.A. Huysmans, T. Hender, B. Alper, Nucl. Fusion 38 179 (1998).
[19]. J.W. Connor, R.J. Hastie, H.R. Wilson, R.L. Miller, Phys. Plasmas 5 2687 (1998).
[20]vB.N. Rogers, J.F. Drake, Phys. Plasmas 6 2797 (1999).
[21]. R.J. Hastie, P.J. Catto, J.J. Ramos, Phys. Plasmas 7 4561 (2000).
[22]. P.B. Snyder, H.R. Wilson et al., Phys. Plasmas 9 2037 (2002).
[23]. A.H. Glasser, J.M. Greene, J.L. Johnson, Phys. Fluids 18 875 (1975).
[24]. J.W. Connor, R.J. Hastie, J.B. Taylor, Proc. Roy. Soc. A 365 1 (1979).
[25]. G.T.A. Huysmans, S.E. Sharapov, A.B. Mikhailovskii, W. Kerner, Phys. Plasmas, 10 4292 (2001).
[26]. S. Saarelma, S. Günter, L.D. Horton, Nucl. Fusion 43 262 (2003).

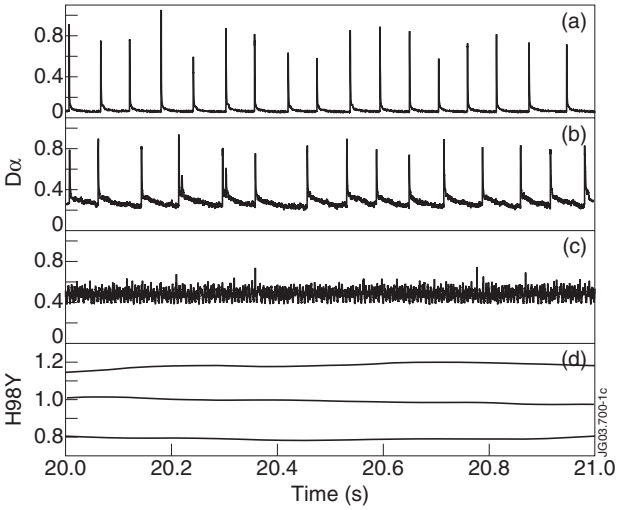

Figure 1: Time traces of D_α emission in JET three JET Pulse no's: (a) 53298, which is a pure type I ELMy H-mode discharge. (b) 53299, which is a mixed type I-II ELMy H-mode discharge. (c) 52739, which is a pure type III ELMy H-mode discharge. Frame(d) shows the confinement factor H98Y as a function of time in same three discharges: 53298 (upper curve), 53299 (middle curve) and 52739 (lower curve).

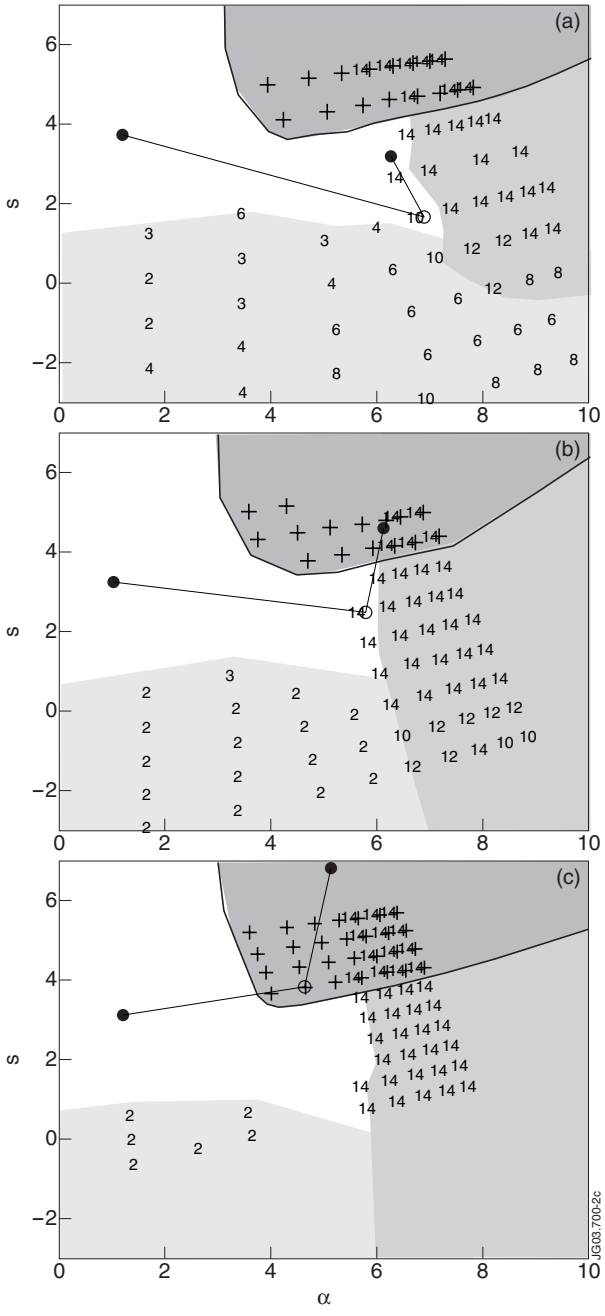

Figure 2:MHD stability diagrams for three predictive JETTO simulations with different levels of external neutral gas fuelling: (a) $\Gamma = 0$,(b) $\Gamma = 4\times10^{22}\ s^{-1}$, (c) $\Gamma = 1\times10^{23}\ s^{-1}$. The numbers on the plot indicate the mode number of the most unstable kin / peeling or ballooning mode. The $n = \infty$ ballooning unstable region has been marked with crosses. The operational point has been plotted for $\rho = 0.92$, $\rho = 0.95$ and $\rho = 0.99$. The location of the top of the ETB at $\rho = 0.95$ has been marked with a circle.

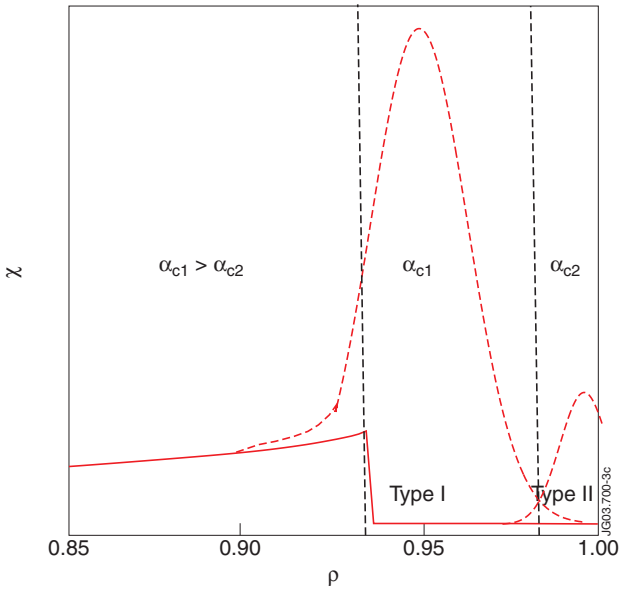

Figure 3: A schematic illustration of the implementation of the model for mixed type I-II ELMy H-mode in JETTO. The ETB has divided into two regions, a narrow edge region for type II ELMs and wider inner region for type I ELMs. In the two regions, different critical pressure gradients are applied and transport is enhanced by Gaussian-shaped perturbations with different amplitudes, widths and centres.

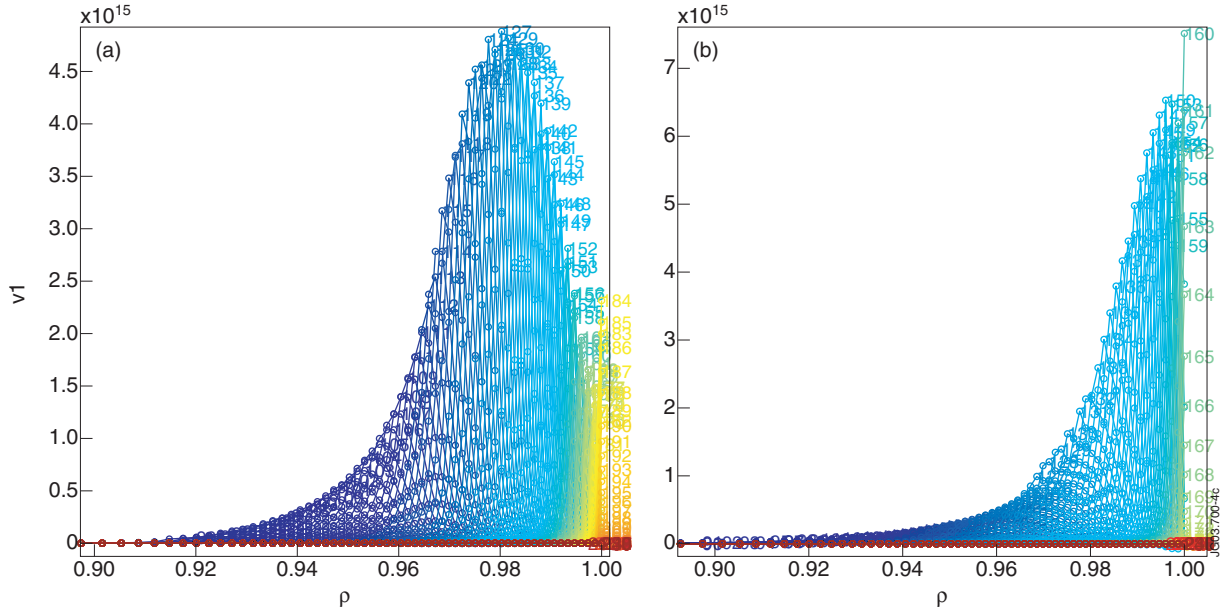

Figure 4: Eigenfunctions of n = 40 ballooning modes in situations with the edge of the pedestal n = ∞ ballooning unstable and the inner part of it second ballooning stable. (a) The edge unstable from ψ = 0.935 to ψ = 1.000, i.e. most of the pedestal unstable. (b) The edge unstable from ψ = 0.990 to ψ = 1.000.

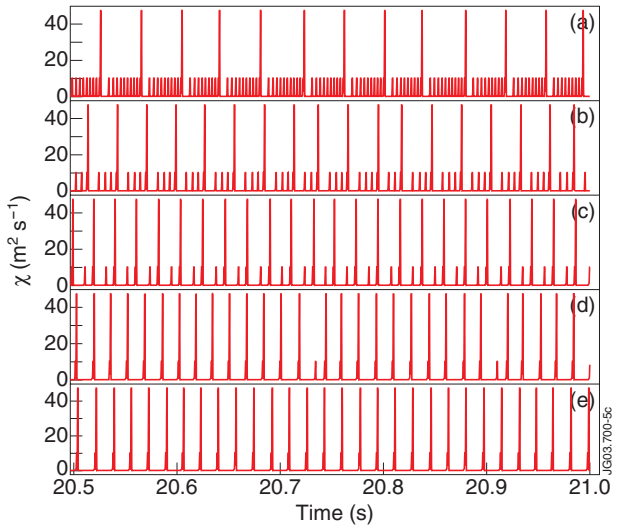

Figure 5: Ion thermal conductivity as a function of time in simulations of mixed type I-II ELMy H-mode with varying type II ELM width. Here, $\alpha_{c,I} = 6.5$ in the inner region of the ETB and $\alpha_{c,II} = 2.5$ in the outer region. The thermal conductivities are enhanced to a maximum level of $100m^2s^{-1}$ and $10m^2s^{-1}$, respectively, during the ELMs, the charac-teristic widths of the Gaussian-shaped perturbations are 4.0cm and 1.0cm, respectively and the centres of the perturbations are $\rho = 0.965$ and $\rho = 0.995$, respectively, in the inner and outer regions of the ETB. The type II ELM width varies as follows: (a) 1.0cm, (b) 1.5cm, (c) 2.0cm, (d) 2.5cm and (e) 3.0cm.

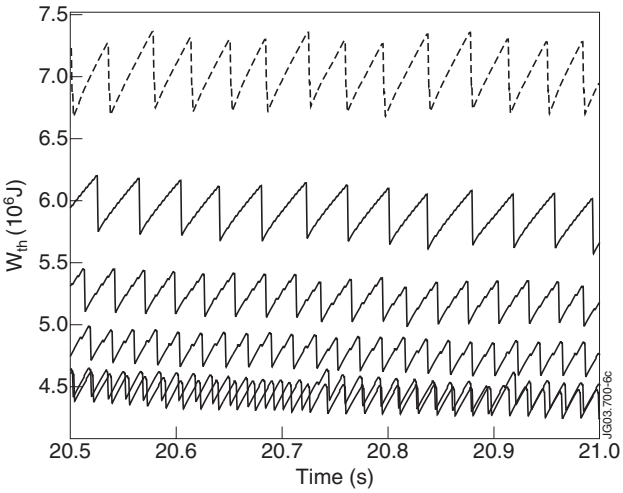

Figure 6: The thermal energy content as a function of time for the simulations in Fig.5 with varying type II ELM width. The solid curves in the figure correspond to type II ELM widths 1.0cm, 1.5cm, 2.0cm, 2.5cm and 3.0cm, from top to bottom. The dashed curved represents a reference simulation of pure type I ELMy H-mode with simulation parameters corresponding to the series of simulations with mixed type I-II ELMs.

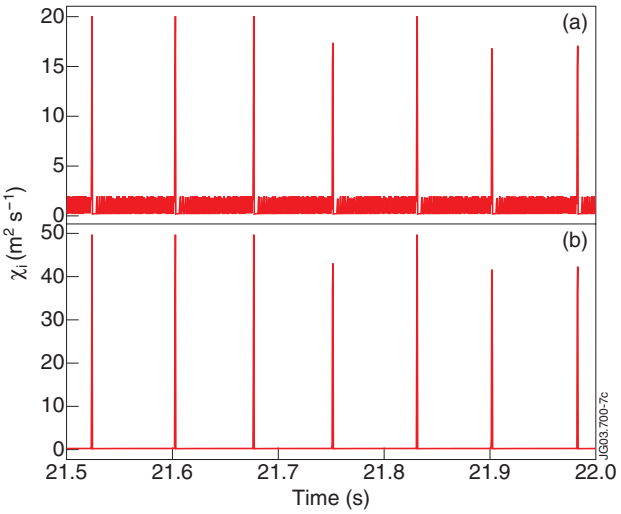

Figure 7: Ion thermal conductivity as a function of time in a typical simulation of mixed type I-II ELMy H-mode at (a) $\rho = 0.995$,(b) $\rho = 0.965$. Here, $\alpha_{c,II} = 6.0$ in the inner region of the ETB and $\alpha_{c,II} = = 3.0$ in the outer region. Ion and electron thermal conductivity during the ELMs is enhanced to a maximum level of $50m^2s^{-1}$ and $2m^2s^{-1}$, in the inner and outer regions of the ETB, respectively. The characteristic widths of the Gaussian- shaped perturbations are 4.0cm and 1.0cm and the centres of the perturbations are at $\rho = 0.965$ and $\rho = 0.995$ in the inner and outer regions of the ETB, respectively.

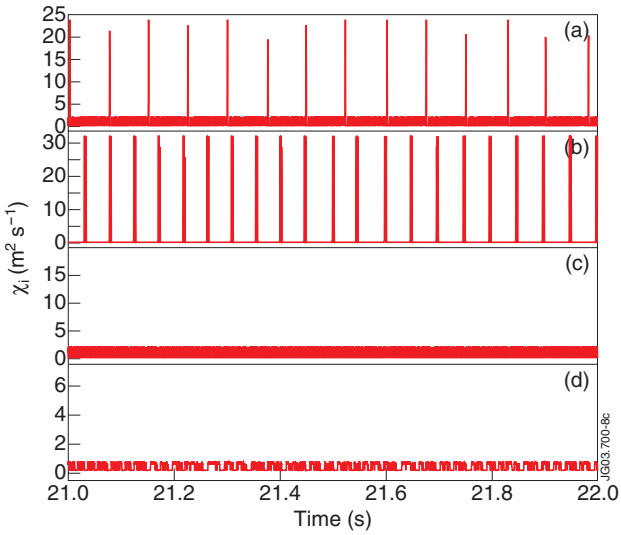

Figure 8: Ion thermal conductivity as a function of time at the magnetic surface $\rho = 0.99$ in four reference simulations of (a) mixed type I-II ELMy H-mode, (b) pure type I ELMy H-mode, (c) pure type II ELMy H-mode and (d) pure type III ELMy H-mode.

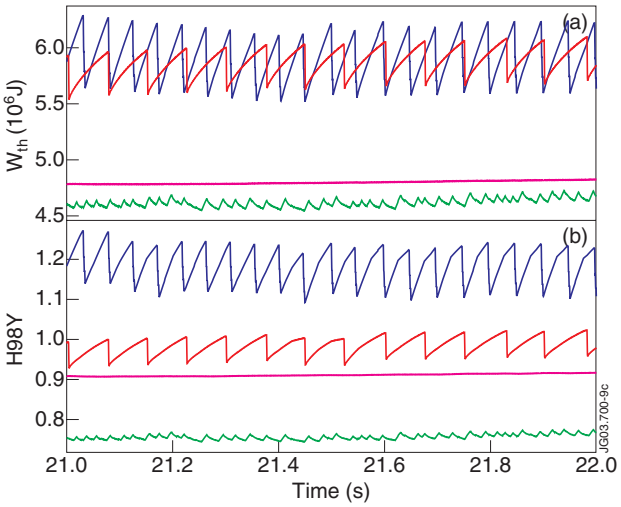

Figure 9: (a) Thermal energy content and (b) confinement factor H98Y as a function of time in the four reference simulations of mixed type I-II ELMy H-mode (red curve), pure type I ELMy H-mode (blue curve), pure type II ELMy H-mode (magenta curve) and pure type III ELMy H-mode (green curve).

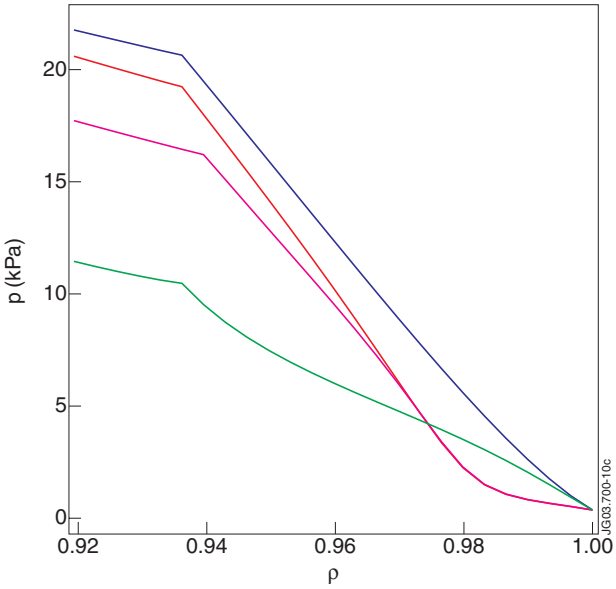

Figure 10: The pressure profiles in the near-pedestal region in four reference simulations of mixed type I-II ELMy H-mode (red curve), pure type I ELMy H-mode (blue curve), pure type II ELMy H-mode (magenta curve) and pure type III ELMy H-mode (green curve). In each case, the pressure profile corresponds to the situation shortly before an ELM. In the particular case of mixed type I-II ELMy H-mode, the pressure profile corresponds to the situation shortly before a type I ELM.

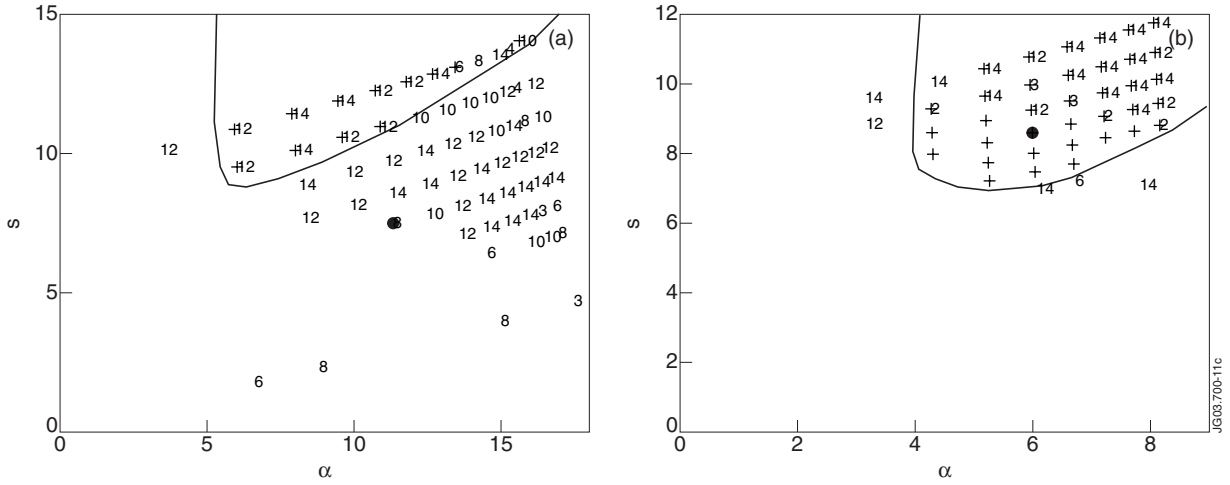

Figure 11: MHD stability diagrams indicating the mode numbers of the most unstable kink, peeling or ballooning modes for a number of locations in the α-s space as well as the n = ∞ ballooning unstable region and the operational point for the magnetic surface ρ = 0.99 for two interpretative JETTO simulations of JET Pulse No's: (a) 55973 with type I ELMs and (b) 56044 with mixed type I-II ELMs.

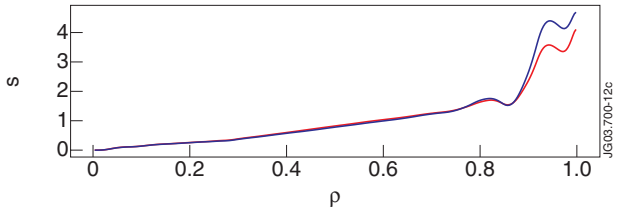

Figure 12: Radial profiles of magnetic shear in two interpretative JETTO simulations with different magnetic configurations. The upper curve at the edge corresponds to a simulation with a single null magnetic configuration taken from JET Pulse No: 53703 and the lower curve at the edge to a simulation with a quasi double null magnetic configuration taken from the same discharge at a later time. The density and temperature profiles are exactly the same in both simulations.

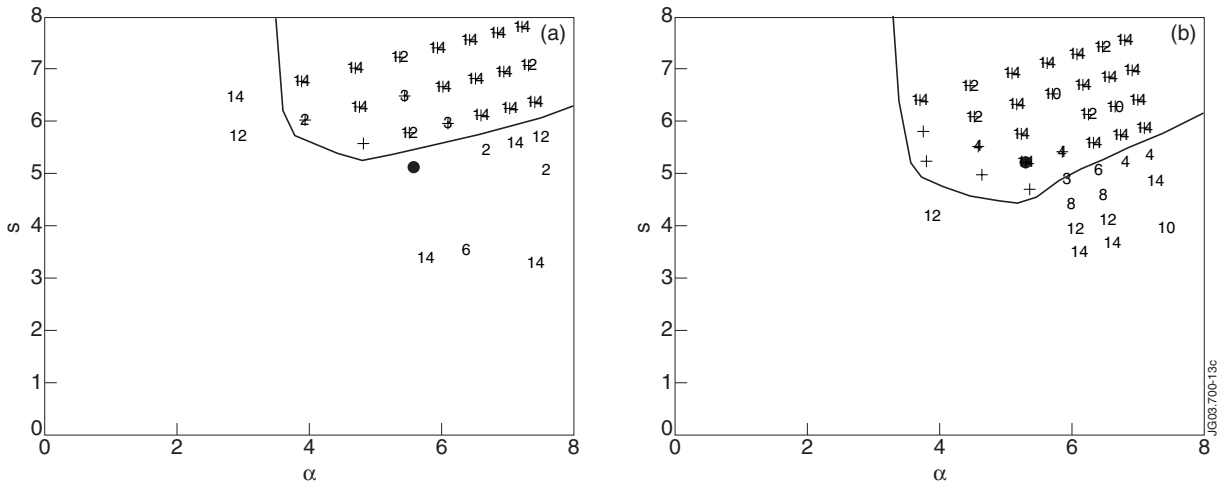

Figure 13: MHD stability diagrams indicating the mode numbers of the most unstable kink, peeling or ballooning modes for a number of locations in the -s space as well as the $n = \infty$ ballooning unstable region and the operational point for the magnetic surface $\rho = 0{:}98$ for two interpretative JETTO simulations of JET Pulse No's: (a) 56044 with a single null magnetic configuration and (b) 56083 with a quasi double null magnetic configuration.

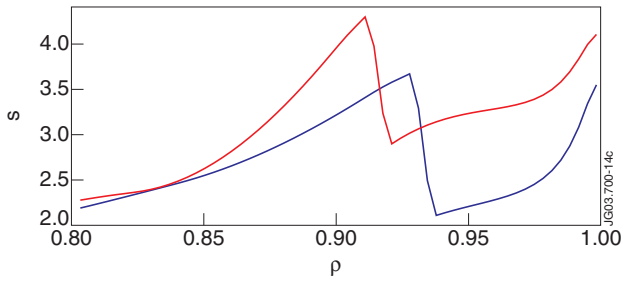

Figure 14: Radial profiles of magnetic shear, when the plasma has evolved for 1.0s in H-mode, in two predictive JETTO simulations, the simulation parameters of which differ only with respect to the level of β_p. Here, the upper curve corresponds to $\beta_p = 2.6$ and the lower curve to $\beta_p = 1.3$.

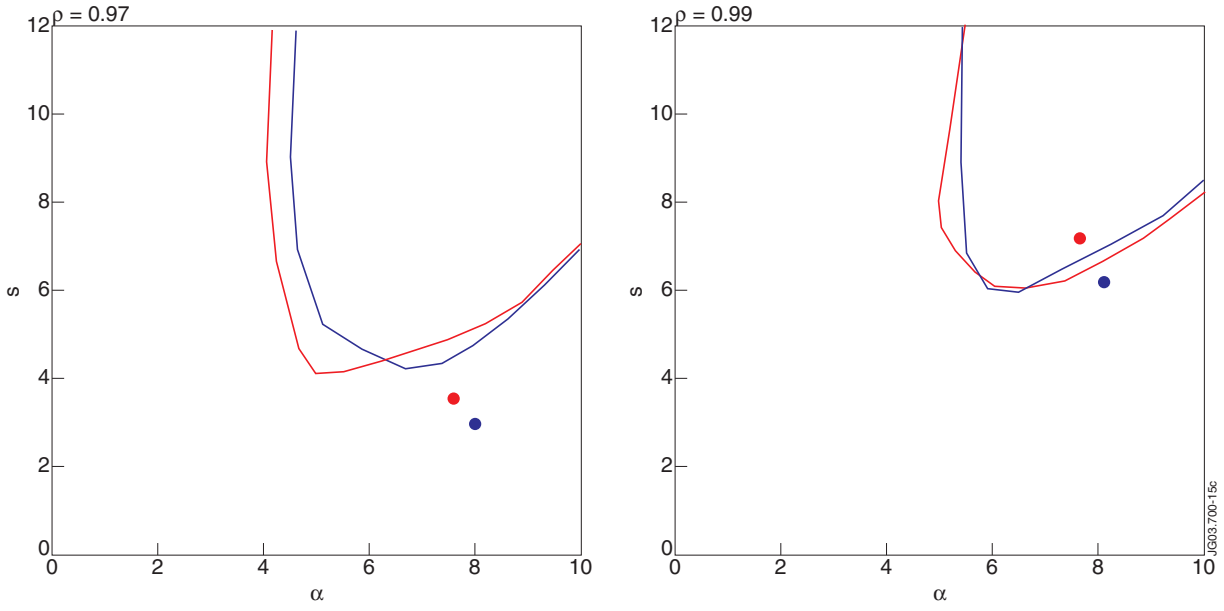

Figure 15: Ideal n = ∞ ballooning stability diagrams for the two predictive JETTO simulations with $\beta_p \approx 1.3$ (blue curve) and $\beta_p \approx 2.6$ (red curve) showing the n = ∞ ballooning stability boundary and the operational point for the magnetic surfaces $\rho = 0.97$ and $\rho = 0.99$.

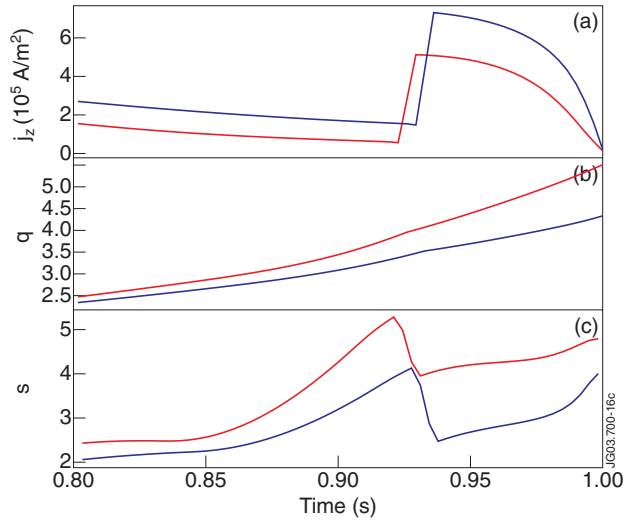

Figure 16: Radial profiles of (a) the total current density, (b) the safety factor and (c) magnetic shear, when the plasma has evolved for 0.5s in H-mode, in two predictive JETTO simulations, the simulation parameters of which differ only with respect to the total current. Here, the red curves correspond to the total current I = 2.1MA and the blue curves to I = 2.5MA.

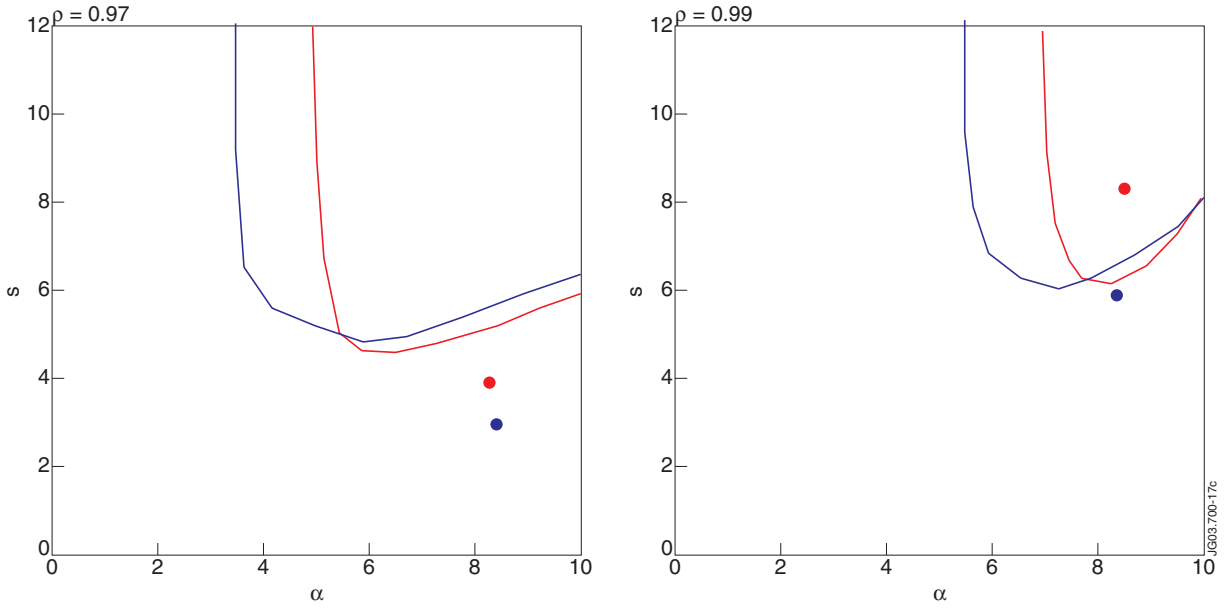

Figure 17: Ideal n = ∞ ballooning stability diagrams for the two predictive JETTO simulations with different total currents and q_{95} = 3.69 (blue curve) and q_{95} = 4.25 (red curve) showing the n = ∞ ballooning stability boundary and the operational point for the magnetic surfaces ρ = 0.97 and ρ = 0.99.

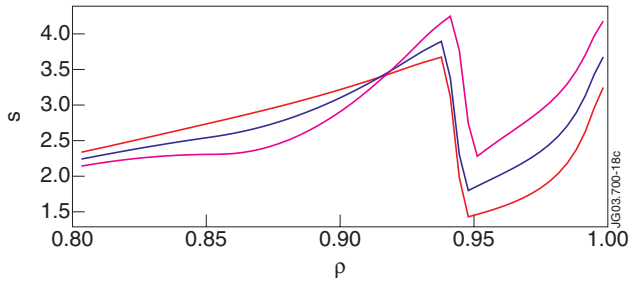

Figure 18: Radial profiles of magnetic shear, when the plasma has evolved for 0.5s in H-mode, in three predictive JETTO simulations, the simulation parameters of which differ only with respect to the triangularity. Here, the lower curve within the ETB corresponds to $\delta = 0.3$, the middle curve within the ETB to $\delta = 0.4$ and the upper curve within the ETB to $\delta = 0.5$.